Original Research Paper

Zinc-doped Prussian blue nanoparticles for mutp53-carrying tumor ion interference and photothermal therapy

Quanyi Jin [a], Wenbao Zuo [a], Qian Lin [a], Ting Wu [b], Cong Liu [b], Nian Liu [a], Jinxue Liu [a], Xuan Zhu [a,]*

[a] *Fujian Provincial Key Laboratory of Innovative Drug Target Research, School of Pharmaceutical Sciences, Xiamen University, Xiamen 361005, China*
[b] *Cancer Research Center, School of Medicine, Xiamen University, Xiamen 361000, China*

A B S T R A C T

Quite a great proportion of known tumor cells carry mutation in TP53 gene, expressing mutant p53 proteins (mutp53) missing not only original genome protective activities but also acquiring gain-of-functions that favor tumor progression and impede treatment of cancers. Zinc ions were reported as agents cytocidal to mutp53-carrying cells by recovering p53 normal functions and abrogating mutp53. Meanwhile in a hyperthermia scenario, the function of wild type p53 is required to ablate tumors upon heat treatment hence the effects might be hindered in a mutp53 background. We herein synthesized zinc-doped Prussian blue (ZP) nanoparticles (NPs) to combine Zn^{2+} based and photothermal therapeutic effects. An efficient release of Zn^{2+} in a glutathione-enriched tumor intracellular microenvironment and a prominent photothermal conversion manifested ZP NPs as zinc ion carriers and photothermal agents. Apoptotic death and autophagic mutp53 elimination were found to be induced by ZP NPs in R280K mutp53-containing MDA-MB-231 cells and hyperthermia was rendered to ameliorate the treatment *in vitro* through further mutp53 elimination and increased cell death. The combinatorial therapeutic effect was also confirmed *in vivo* in a mouse model. This study might expand zinc delivery carriers and shed a light on potential interplay of hyperthermia and mutp53 degradation in cancer treatment.

1. Introduction

Transcription factor p53, encoded by gene TP53, is one of the most studied cancer-related genes. It reacts to cell stress signals [1] by regulating downstream factors to maneuver cell cycle arrest, DNA repair, apoptosis, metabolism, senescence, etc. [2,3]. Owing to various genome protective and tumor suppressive functions, p53 is referred to as the "Guardian of the Genome" [4]. Over half of known cancers, however,
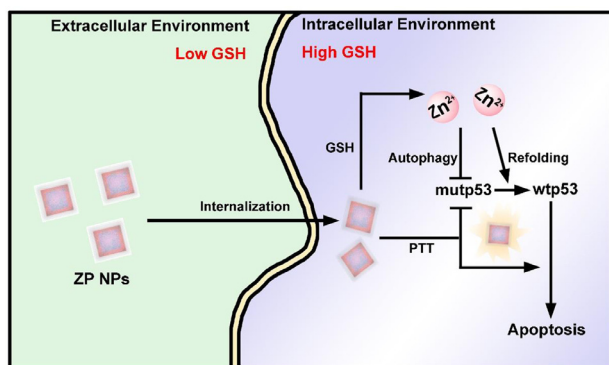
Scheme 1 – The combinational effects of ion interference and photothermal treatment of ZP NPs.

exhibit a mutated form of p53 (mutp53) [5–7], and a large proportion of missense and nonsense mutations not only annihilate the normal physiological functions of p53, but support the development of cancer by endowing new gain-of-functions (GOF) including proliferation, metastasis, metabolism remodeling and resistance to various therapy [7–11], further threating the health of patients and thwarting cancer treatments.

The fact that tumor progression relies on mutp53 with GOF [12–14] posits mutp53 a drug target to treat cancer [15,16]. Agents have been found and reported to degrade mutp53 via proteasome (arsenic compounds, statins, NSC59984, 17-AAG and ganetespib) [17–21], or through autophagy (MCB-613, SAHA, gambogic acid and capsaicin) [22–25]. Zn^{2+} has also been found to be an effective agent. Since mutp53 is prone to lose Zn^{2+} required in active center and subsequently to misfold and aggregate [26], supplementation of zinc has been shown to recover wild type p53 (wtp53) functions [27] and trigger degradation of harmful and redundant mutp53 [28,29]. Although ion interference therapy with body-constituting metal ions like Zn^{2+} is convenient and effective, specific delivery methods are required to circumvent physiological homeostasis and efficiently regulate ion levels of target sites [30]. ZnO was first found to be more effective in killing mutp53 carrying cells than those with wild type p53 and p53 knockdown [31]. Especially designed Zn^{2+} carriers include a zinc-chelator complex, Zn(II)-curc, which reactivated missing p53 functions [32] and trigger mutp53 degradation via endoplasmic reticulum (ER) stress [33] and subsequent autophagy [29]. Another group fabricated nanosized ZnFe-4 particles [34] and peptide-modified ZIF-8 particles [35], and both manifested proteasomal degradation of mutp53. The safety of zinc delivery methods remains to be improved and further zinc carriers still await exploitation. In addition, the selection of degradation pathway in a zinc interference scenario remains unclear.

Hyperthermia is another long-lasting hot keyword in tumor therapy [36], and wtp53 was reported to respond to heat signal and hence played a role in hyperthermia cancer therapy, where mutp53 mitigated the therapeutic effect [37]. Although a few studies revealed heat-compromised mutp53 levels [38], little has been investigated on how hyperthermia

and zinc ion interference therapy might interplay with each other, especially in a tumoricidal context. We herein seek to design a nano-sized carrier combining Zn^{2+} delivery and hyperthermia production. Hence, we selected Prussian blue (PB) for (1) its biosafety manifested by FDA-approved clinical application in cesium and thallium elimination (Radiogardase® from fda.gov) [39,40], (2) its outstanding photothermal conversion efficiency [41] and potential as a photothermal therapeutic agent [42], and (3) its relatively facile largescale preparation of nanoparticles (NPs). Although works have been carried out to harness PB as ion carriers of metal ions including Cu^{2+} [43,44] and Mn^{2+} [45], but limited attempt has been made to deliver Zn^{2+} with PB NPs.

In this work, we were able to fabricate zinc-doped Prussian blue nanoparticles (ZP NPs) by substituting iron of already prepared PB NPs with free Zn^{2+} with an unscathed photothermal effect. The construct, with a capability to degrade and release zinc ions in a neutral and GSH rich environment, could be deemed as a Zn^{2+} delivery carrier. Furthermore, ZP NPs induced death of model mutp53-expressing cells, MDA-MB-231, and drastically downregulated their mutp53 levels via autophagy (Scheme 1). Both cytotoxicity and mutp53 destabilization effects were further expanded with laser triggered hyperthermia and combination of ZP and photothermal treatment achievement an ideal tumoricidal results in a mouse model. These findings might provide clues to mutp53 ablation and photothermal therapy in cancer treatment and rendered PB as a promising carrier in Zn based ion interference therapy.

2. Materials and methods

2.1. Materials

Poly(vinylpyrrolidone) (PVP K30), ferricyanide ($K_3[Fe(CN)_6]\cdot 3H_2O$), hydrogen chloride (HCl), zinc acetate ($Zn(OAc)_2$), trisodium citrate ($Na_3(C_6H_5O_7)\cdot 2H_2O$), monosodium phosphate, disodium phosphate and glutathione (GSH) were purchased from Aladdin Reagent, Ltd (Shanghai, China). Dulbecco's modified Eagle medium (DMEM) was purchased from Cytiva (USA). Fetal bovine serum (FBS) was purchased from ABW (China). Penicillin-streptomycin stock solution was purchased from Beyotime Biotechnology (China), Calcein-AM/Propidium Iodine (PI) Live/Dead Cell Double Staining Kit was purchased from Bestbio (China). Annexin V-FITC/PI Apoptosis Detection Kit was purchased from 4A Biotech (China). Anti-rabbit GAPDH antibody (10494–1-AP) was purchased from Proteintech Group (USA). Anti-rabbit mutant p53 antibody (mutp53, Y5, ab32049) and HRP conjugated anti-rabbit IgG secondary antibody (ab6721) were purchased from Abcam (USA).

2.2. Preparation of ZP NPs

First, PB NPs was fabricated with a typical hydrothermal method. 790.2 mg $K_3[Fe(CN)_6]\cdot 3H_2O$ and 9 g PVP were magnetically stirred in 120 ml deionized water with 10 mM HCl to a clear yellow solution, heated to 80 °C for 20 h, and aged

at room temperature for 24 h. Then, PB NPs were obtained from resulting solution with centrifugation, washed with deionized water for 3 times, and dried at 60 °C for 2 h. Next, PB NPs, Zn(OAc)$_2$, PVP and Na$_3$(C$_6$H$_5$O$_7$)·2H$_2$O are mixed and magnetically stirred in water at a 1:2:2:1.35 mass ratio for 4 h, and further stirred with addition of K$_3$[Fe(CN)$_6$]·3H$_2$O at 1/4 mass of original PB NPs for another 1 h. Finally, the mixture was aged for 24 h and ZP NPs were collected via centrifugation and washed with ethanol and water for 3 times.

2.3. Characterizations

The sizes and morphologies of NPs were observed and imaged with transmission electron microscopy (TEM, Tecnai G2 Spirit BioTWIN, FEI, Holland, and HT-7800, Hitachi, Japan) and scanning electron microscopy (SEM, GeminiSEM 500, Zeiss, Germany). Elemental and structural analyses of NPs were further carried out with SEM based energy-dispersive spectrometry (EDS) and elemental mapping, ultraviolet-visible (UV–vis) absorbance spectra (UV- 2550, Shimadzu, Japan), X-ray photoelectron spectroscopy (XPS, Escalab Xi+, Thermo Fisher Scientific, USA), and X-ray diffractometry (XRD, XRD-7000, Shimadzu, Japan). All quantification of metal is carried out with inductively coupled plasma optical emission spectrometry (ICP-OES, SPECTROBLUE FMX36, SPECTRO, Germany).

2.4. Ion release

NPs are confined in 3.5 kMW dialysis bags and soaked in 20 mM phosphate buffers with corresponding pH values and GSH concentrations to an indicated final NP concentration. The solutions were shaken at 37 °C and sampled at each time point, and the metal ion concentrations of samples were measured with ICP-OES. TEM images were also taken after soaking NPs in corresponding buffer solutions for 12 h.

2.5. Photothermal effect evaluation

200 μl water and various concentration of NP suspensions were irradiated with varied power densities of 808 nm laser, and the temperature changes were detected via a thermocouple thermometer (TES1310, TES electronics industry Co. Ltd. China). In each heat-cooling cycle, the material dispersion was irradiated with 1.0 W/cm^2 808 nm laser for 6 min (ON) and allowed to naturally cool down to room temperature (OFF, also 6 min in the study).

2.6. Cell culture

Human breast cancer cells MDA-MB-231 were purchased from American Type Culture Collection (ATCC, MD, USA). Cells were cultured in a humidified 37 °C and 5% CO$_2$ atmosphere in DMEM supplemented with 10% FBS and 1% penicillin-streptomycin antibiotics.

2.7. Cellular cytotoxicity and apoptosis

Cells were seed in 12-well plates at a density of ∼5 × 10^5 cells per well, and were treated with NP suspensions with or without inhibitors for 8 h (apoptosis) or 24 h (live/dead double staining). In PTT groups, cells were irradiated 4 h after treatment with laser at corresponding power density for 4 min. Cells were harvested and wash with PBS twice and stained following protocols in the kits and analyzed with flowcytometry (ATTUNE 22 NXT, Thermo Fisher Scientific, USA).

Confocal scanning laser microscopy (CLSM) was conducted to live/dead double stained cells 16 h after treatment.

2.8. Intracellular uptake

ZP NPs were labeled with ICG by mixing 1 mg NPs with 5 ml ICG water solutions (1 mg/ml) and incubated overnight. The resulting NPs were collected and washed with water. 6-well plate seeded cells were treated with 100 μg/ml labeled ZP NPs and harvested at each time point to allow flowcytometric analysis. Cells were also treated with 100 μg/ml ZP NPs for Zn element measurement. Harvested cells were counted and digested with concentrated nitric acid and hydroperoxide for ICP-OES quantification.

2.9. Western blotting

Cells lysates were obtained from 8 h treated cells. Proteins from lysates were isolated with 10% SDS-PAGE gels, transferred onto PVDF membranes, and blotted with primary and secondary antibodies. The membranes were imaged with Tanon 5200S (Tanon, China).

2.10. Animals and tumor models

All animal experiments followed protocols approved by the Institutional Animal Care and Use Committee of Xiamen University. 4–6-week-old Female Balb/c nude mice were purchased from Shanghai SLAC laboratory Animal Co., Ltd. MDA-MB-231 cells was subcutaneously planted in the right thigh position of mice at a density of ∼1 × 10^7. All experiments were conducted after tumor growth for 1 week. The volumes of tumors were measured follow $V = L \times W^2/2$, with L and W designating the lengths and widths of tumors, respectively.

2.11. In vivo fluorescent imaging

The tumor bearing mice were intravenously injected with ICG-labeled ZP NPs (dose 6.25 mg/kg). The fluorescent images were collected at various time points with an animal imager (Caliper IVIS Lumina II, USA).

2.12. In vivo infrared thermal imaging

The tumor bearing mice were injected with saline, PB and ZP NPs (both at a dose of 6.25 mg/kg) intravenously. After 24 h, tumor sites of each group were irradiated with 808 nm laser with a power density of 1.0 W/cm^2 for 5 min. The thermal images were taken and real-time temperature was recorded every minute with near-infrared thermography (AVS-C528, China).
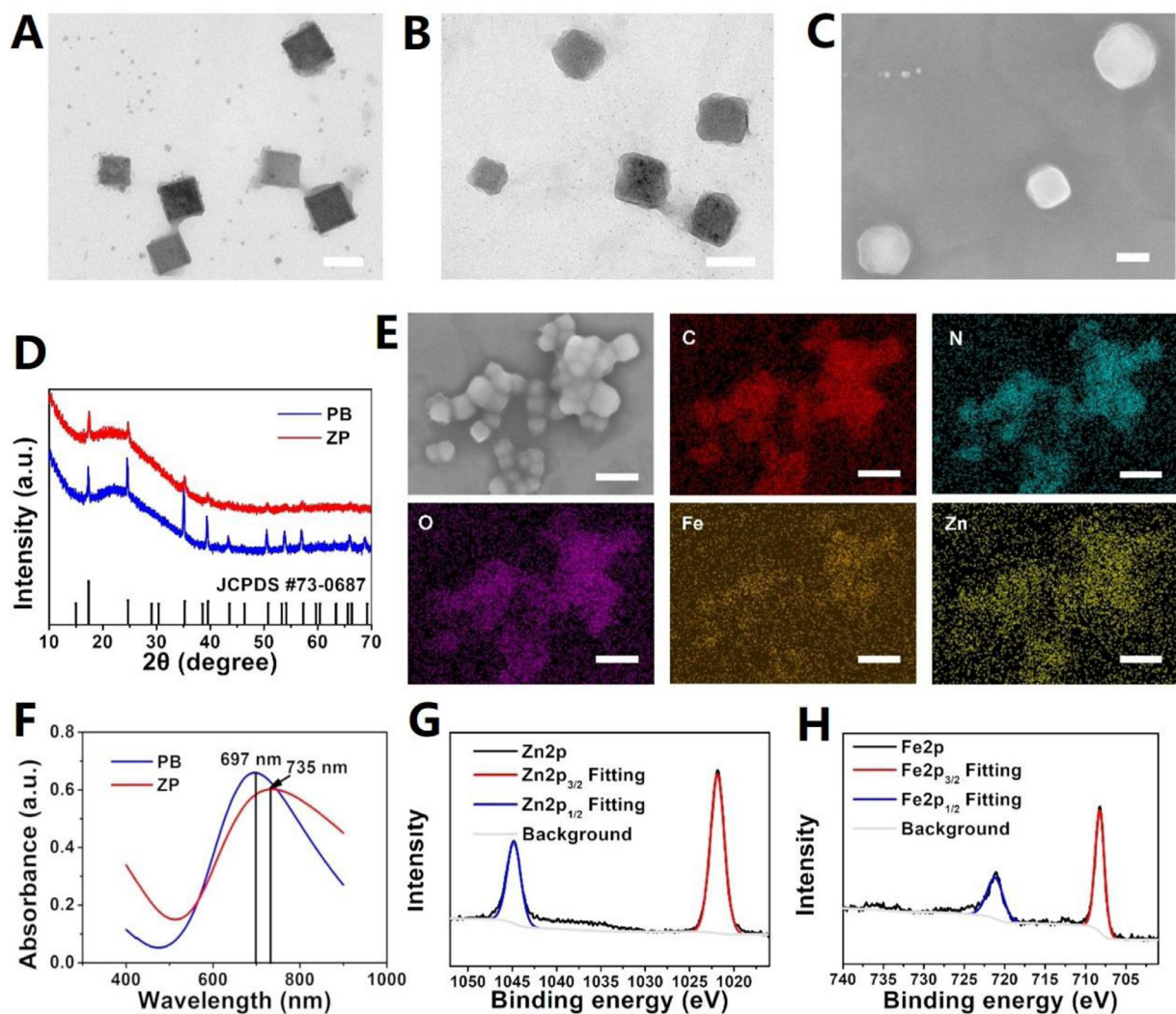
Fig. 1 – Preparation and characterization of PB and ZP NPs. Representative TEM images of (A) PB NPs and (B) ZP NPs, and (C) SEM image of ZP NPs. Scale bars:100 nm. (D) XRD spectra of PB and ZP NPs in comparison to standard pattern of PB. (E) SEM-based EDS mapping of ZP NPs. Scale bars:200 nm. (F) UV–vis spectra of PB and ZP NPs. XPS analysis of (G) Zn 2p and (H) Fe 2p.

2.13. In vivo tumoricidal effect investigation

4 treatment groups of mice, saline (NC), PB+laser, ZP and ZP+laser, were randomly assigned ($n=5$). Saline and NPs (dose: 6.25 mg/kg) were injected intravenously every 4 d and laser treatment (808 nm, 1.0 W/cm^2, 5 min) were carried out 24 h post-injection. The tumor sizes and body weights were recorded every 4 d over the entire 2-week treatment period. Tumors weights were measured after sacrifice of mice and tumors and other organs were collected for Hematoxylin and eosin (H&E) staining.

2.14. Statistical analysis

Student's t-test was conducted for statistical analysis and the significance was determined as *$P < 0.05$, **$P < 0.01$ and ***$P < 0.001$.

3. Results and discussion

3.1. Preparation and characterization of ZP NPs

ZP NPs used in this study were prepared with a two-step strategy. Firstly, PB NPs were synthesized with a typical hydrothermal method. $K_3[Fe(CN)_6]$ and PVP were heated in an acidic solution, and, as displayed in TEM and SEM, PB NPs were featured by a cubic shape with sizes around 80–110 nm (Fig. 1A). Combining the XRD data of PB NPs showing characteristic peaks which correspond to the standard pattern of $Fe_4[Fe(CN)_6]_3$ (JCPDS #73–0687) [46], the successful formation of PB structure was further confirmed (Fig. 1D). PB NPs were then stirred in a Zn^{2+} solution to allow ion exchange reaction and ZP NPs were finally obtained. ZP NPs maintained the morphology and sizes of PB NPs except
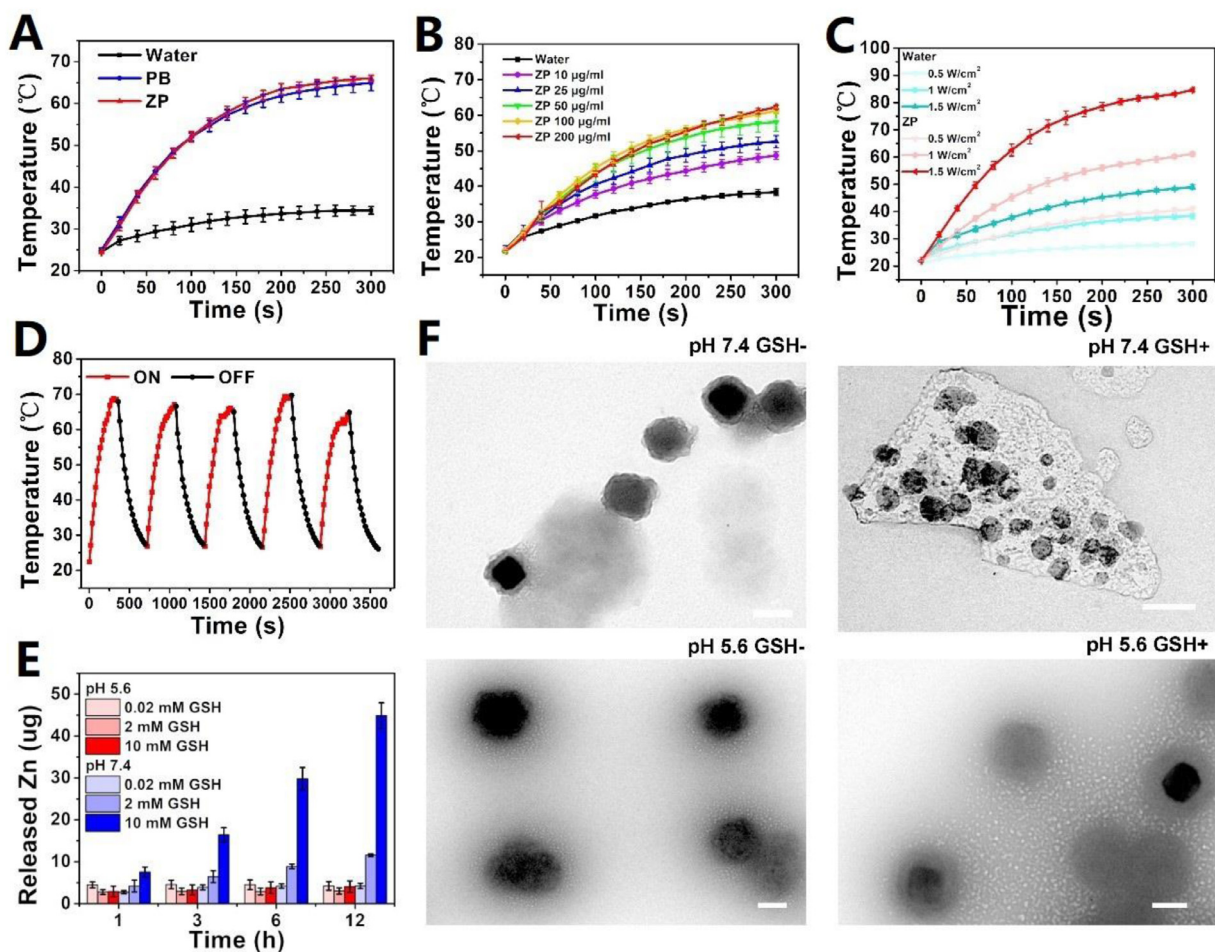
Fig. 2 – PTT performance and Ion releasing profile. (A) Comparing photothermal effects of PB and ZP (both 100 μg/ml, 1.0 W/cm^2). $n = 3$. (B) Concentration dependent (1.0 W/cm^2) and (C) power density dependent (100 μg/ml ZP) photothermal effects of ZP. $n = 3$. (D) photothermal effect changes of ZP in heat-cooling cycles (ZP 100 μg/ml, 1.0 W/cm^2). (E) Zn release of ZP in different pH values with varied concentration of GSH (1.5 mg ZP NPs in 15 ml buffer solutions). $n = 3$. (F) TEM images of ZP NPs incubated in corresponding solutions for 12 h. Scale bars:100 nm.

slightly dented edges of original PB cubes (Fig. 1B and 1C). In the XRD spectra of ZP NPs, the peaks of PB NPs were detected with apparently less intensities without new peaks emerging, indicating partial loss of original PB crystalline structures at the particle surfaces during the random Zn substitution process (Fig. 1D). EDS mapping analysis based on an SEM image rendered a homogenous dispersion of Fe and Zn elements in the particles (Fig. 1E). Additionally, the UV–vis spectra depicted a red shift of the absorption peak after zinc substitution (Fig. 1F), consistent with previous reported results [47], also indicating the existence of Zn^{2+} in PB lattices.

The fabricated ZP NPs were further analyzed with XPS. The XPS survey of ZPs demonstrated the existence of Zn and Fe elements in the particles (Fig. S1). Peaks at 1021.33 eV, 1044.80 eV, 707.94 eV and 721.18 eV match Zn2p$_{3/2}$, Zn2p$_{1/2}$ (Fig. 1G), Fe2p$_{3/2}$ and Fe2p$_{1/2}$ (Fig. 1H), respectively. By calculating ratio of 2p$_{3/2}$ peak areas, the Fe:Zn molar ratio was estimated to be 1:2.7, while when the metal elements were quantified with ICP-OES, the mean zinc mass concentration and the mean Fe:Zn molar ratio of ZP NPs were measured to

be 5.3% and 5.6:1, respectively. Considering the thin surface-probing nature of XPS techniques, the contrasting results of relative Fe/Zn amount suggested that Zn substitution might mainly happen at the surface of PB NPs.

3.2. Photothermal effects of ZP NPs

The photothermal-conversion abilities of PB NPs and ZP NPs were then investigated to confirm photothermal therapeutic potential. Possessing absorption peaks that cover 808 nm wavelength, PB and its analogues are capable of producing heat under the radiation of 808 nm laser. The 5 min irradiation of 1.0 W/cm^2 808 nm laser raised the temperature of 100 μg/ml PB NPs by 39.9 °C, significantly higher than the pure water group (9.9 °C). Under the same condition, ZP NPs exhibited a similar temperature increase (41.6 °C) to the PB group, indicating little detriment to photothermal performance was brought by Zn substitution (Fig. 2A). In addition, the heating efficiency of ZP NPs rose with their concentrations (Fig. 2B) and laser power density (Fig. 2C), elucidating
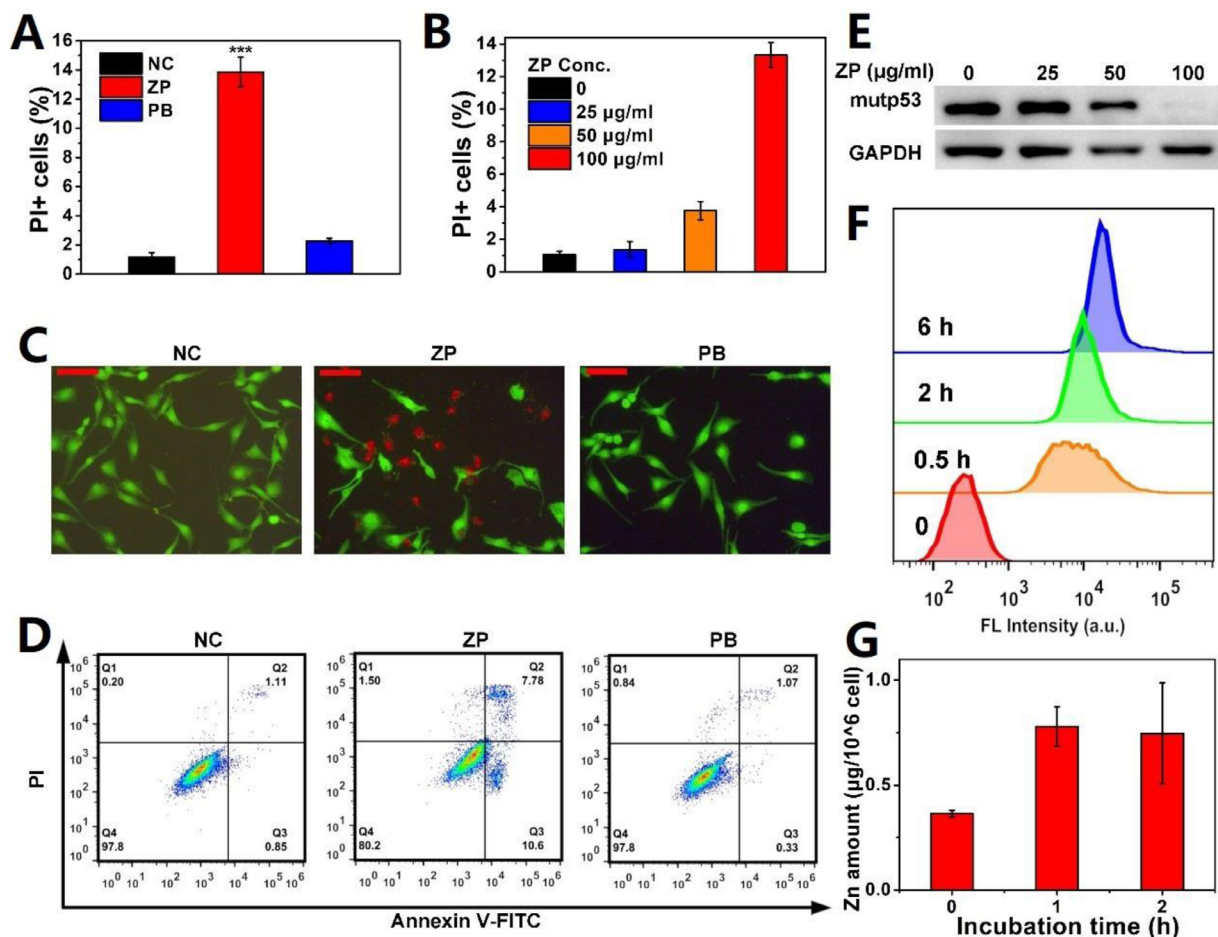
Fig. 3 – *In vitro* ZP treatment on MDA-MB-231 cells. (A) Calculated PI+ cell rates (Q1+Q2) based on flowcytometry analyzed Calcein-AM/PI live/dead double-staining results (100 µg/ml ZP and PB). $n = 3$. ***P <0.001. Student's *t*-test. (B) PI+ cell rates for various concentration of ZP NPs treated cells. $n = 3$. (C) CLSM images of live/dead double stained cells (100 µg/ml ZP and PB). Scale bars, 100 µm. (D) Cell apoptosis. Flowcytometry analysis of annexin V-FITC/PI double-stained cells (100 µg/ml ZP and PB). (E) Western blotting of cell mutp53 after treatment of various concentration of ZP NPs. (F) Flowcytometry analysis of fluorescent positive cells incubated with ICG-labeled ZP NPs. (G) ICP-OES analysis of cell Zn levels after ZP NP incubation.

a concentration- and power-dependent photothermal performance of the material. The photothermal stability of ZP NPs was studied by carrying out 5 heat-cooling cycles (Fig. 2D). The recorded temperature changes depicted little deterioration of photothermal effects, confirming a stable capability of ZP NPs to induce hyperthermia under laser irradiation. The photothermal conversion efficiencies of ZP was measured with the method from another published work of our group [44] and calculated to be 9.9% (Fig. S2).

3.3. ZP NPs release ion in response to GSH concentration

One of the most crucial properties of the ion delivery carrier is releasing ions at the target site, and in this scenario, unloading free Zn^{2+} in intracellular environment of a cancer cell. As cytosol is known of 2 to 3 level higher concentration of GSH than extracellular environment [48], phosphate buffers of pH 5.6 and 7.4 containing various concentrations of GSH are used to incubate ZP NPs to figure out their ion releasing behaviors. Comparing to all acidic groups, a GSH

concentration-dependent Zn^{2+} release was monitored in a 12 h observation (Fig. 2E). The trend was consistent with TEM images of ZP NPs receiving corresponding treatments, where NPs in acidic solutions and the GSH free neutral solution maintained their initial sizes with only mild morphological changes after 12 h but those in the GSH addition neutral group collapsed into debris of smaller sizes and random shapes (Fig. 2F). The ion releasing behavior was also investigated with or without laser irradiation treatment, and photothermal effects didn't seem to affect the release of Zn^{2+} in any of the studied media (Fig. S3). The results indicated that GSH-enriched cytoplasm of cancer cells might be where ZP NPs break apart once internalized. Meanwhile, as released Zn^{2+} in a large amount is the basis of a successful ion interference, this process enables further function of delivered intracellular Zn^{2+}.

GSH, with reported chelating ability and affinity to Zn^{2+} might be responsible for the ion release. The ion binding ability of GSH increases with pH rising above 6.0 when a carboxyl group provides an extra coordination site via
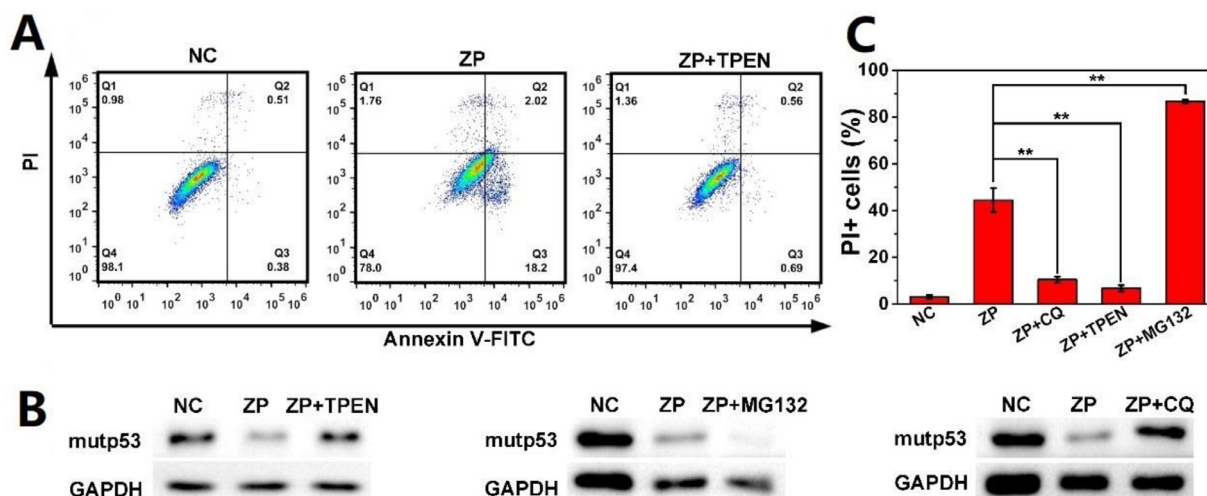
Fig. 4 – Effects of inhibitors on ZP treatment. (A) Apoptosis of cells treated with ZP (100 µg/ml) and TPEN (10 µM). (B) Western blotting of ZP-treated cell mutp53 with or without addition of TPEN (10 µM), MG-132 (10 µM) and CQ (15 µM). (C) PI+ cell rate for ZP and inhibitors treated cells (100 µg/ml ZP, 10 µM MG-132, 15 µM CQ, 10 µM TPEN). $n = 3$. **$P < 0.01$. Student's t-test.

ionization [49], consistent with observed higher Zn^{2+} release in our experiment.

3.4. ZP NPs induce MDA-MB-231 cell death and mutp53 degradation

MDA-MB-231 breast cancer cell, containing R280K mutation in p53, was chosen as a model cell line to investigate the potential antitumor bioactivity of ZP NPs. Calcein-AM/PI live/dead double staining assay was performed 24 h after corresponding treatments. According to the flowcytometry results, 100 µg/ml PB NPs applied a negligible impact on the survival of cells, exhibiting their ideal safety as a biomaterial. While an equivalent amount of ZP NPs induced significant cell death in comparison (Fig. 3A and S4) and the cytotoxicity displayed concentration dependency (Fig. 3B and S5). The similar trend could also be depicted in CLSM image of live/dead double stained cells (Fig. 3C). As demonstrated further in the Annexin V-FITC/PI staining assays, the consistent results to live/dead staining could elucidate that ZP-triggered cell death was apoptotic (Fig. 3D). Since in mutp53 containing cell lines, cell growth relies on mutp53, such that abrogation of mutp53 would compromise cell survival. The mutp53 degradation ability of Zn^{2+} should be consistent with the cell survival results [29,34,35]. As expected, ZP delivered Zn^{2+} exhibited a dose dependent mutp53 depletion ability, as shown in Western blotting (WB) images (Fig. 3E).

Zn-doped version of PB, in comparison with relatively safe PB, appear to be toxic to MDA-MB-231 cells. To render the toxicity of Zn^{2+}, ZP NPs are supposed to be firstly internalized by cells and elevate the intracellular Zn levels. The internalization was tested with ICG-labeled ZP NPs. The fluorescent signal positive cell count increase in 6 h was measured with flowcytometry, indicating gradual population growth of successful NP uptake cells (Fig. 3F). The intercellular Zn levels were monitored with ICP-OES for

the first 2 h after ZP incubation and a drastically increased Zn amount was observed in the ZP group (Fig. 3G), also indicating efficient uptake of ZP NPs by cells. Furthermore, a cell permeable Zn^{2+} specific chelator, N,N,N',N'-Tetrakis(2-pyridylmethyl)ethylenediamine (TPEN), was introduced to the study. TPEN was considered to deplete intracellular Zn level with its affinity to Zn^{2+} and was widely used in the research of Zinc-related functions. The toxicity of ZP was shown to be dependent on the elevated zinc level *per se*, since the addition of TPEN, significantly neutralized ZP induced apoptosis (Fig. 4A and 4C) and the degradation of mutp53 (Fig. 4B).

3.5. ZP-Triggered cell death and mutp53 depletion are autophagy dependent

The mutp53 levels of MDA-MB-231 cells co-treated with ZP and potential inhibitors were investigated with WB. An autophagy inhibitor, chloroquine (CQ), recovered ZP induced mutp53 degradation, while the co-treatment with a proteasome inhibitor, MG132, accelerated the mutp53 elimination on the contrary (Fig. 4B). The mutp53 degradation in this scenario followed an autophagy dependent pathway, and the MG132 treatment result is consistent with one of its reported functions as an autophagy activator [50].

The survival of cells was supportive to the result. CQ protected cells against the challenge of ZP while MG132 exacerbated the cell death (Fig. 4C), interpreting that ZP induced cell death relies on autophagy, and autophagic protein degradation might plays an important role.

3.6. Combinational effect of ZP NPs and photothermal treatment

Having witnessed the Zn^{2+} dependent cytotoxicity of ZP, we attempted to figure out the potential combinational effect of ZP treatment and laser induced hyperthermia. In the unsubstituted PB group, neither mere PB treatment nor
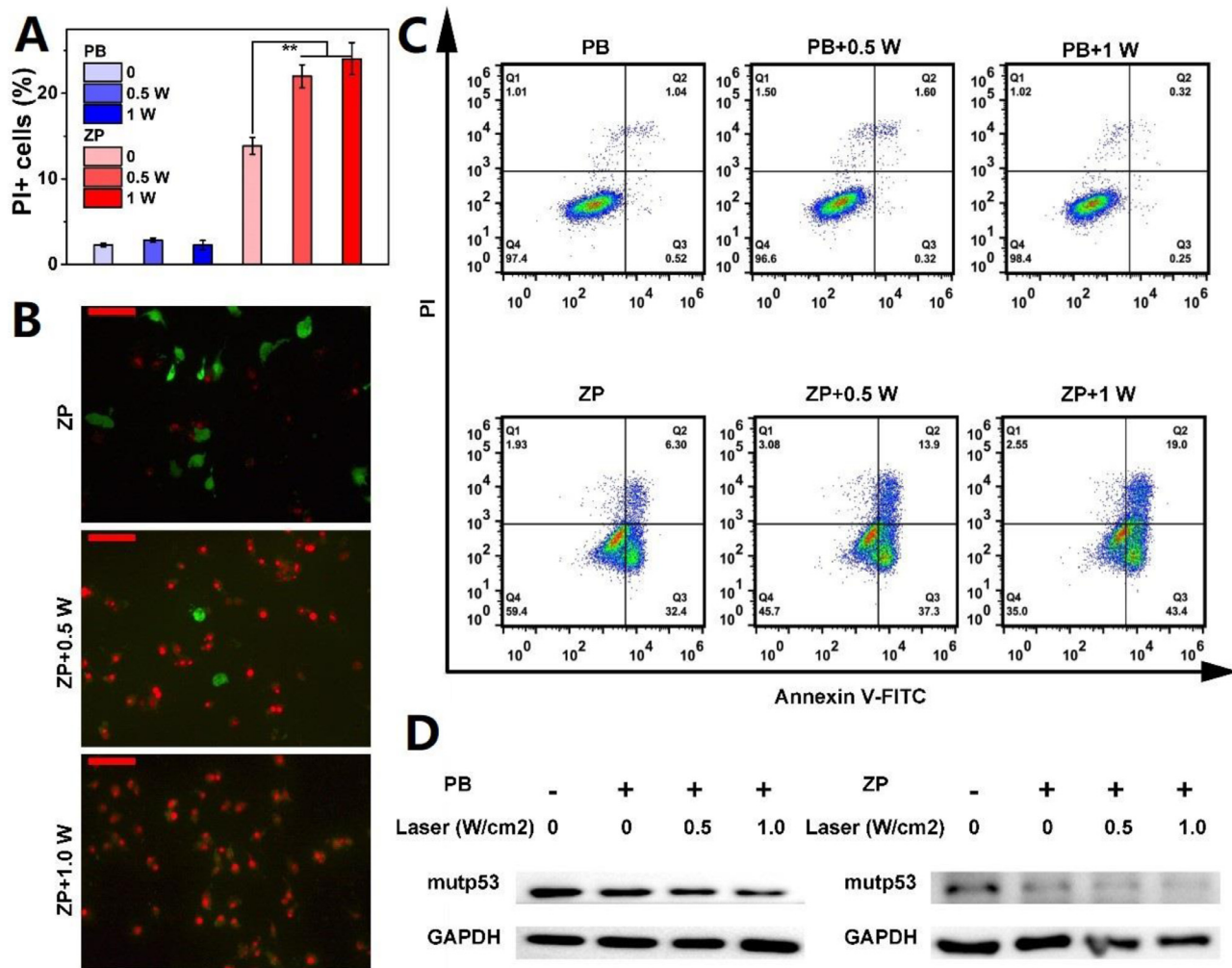
Fig. 5 – Combinational effects of ZP and laser irradiation. (A) Calculated live/dead double-stained PI+ cells and upon PB/ZP treatment (both 100 μg/ml) with or without laser irradiation. $n = 3$. ** P <0.01. Student's t-test. (B) Representative CLSM images. Scale bars, 100 μm. (C) Cell apoptosis upon PB/ZP treatment (both 100 μg/ml) with or without laser irradiation. (D) Western blotting of cell mutp53 levels upon above NP with or without laser treatment.

PB+laser irradiation at the current experimental condition caused apparently detectable cell death. In contrast, the same laser treatment to ZP groups seemed to further elevated the ZP NP-induced cell death rate (Fig. 5A, 5C and S6). Consistent results were also shown in CLSM images taken from ZP+laser treatment cells (Fig. 5B).

Meanwhile, mutp53 level changes were also investigated through WB. PB caused hyperthermia, although failed to lead to significant cell death, slightly destabilized mutp53 at least in R280K expressing MDA-MB-231 background (Fig. 5d left). Similar results have been reported in other PTT scenarios [38,51], where mutp53 was downregulated at a transcriptional level, different from the direct degradation of mutp53 proteins triggered by Zn [34,35]. The mutp53 in the irradiated ZP groups, concordantly, was further degraded due to both effects of Zn^{2+} and heat (Fig. 5d right). The photothermal treatment alone might trigger mutp53 degradation insufficient to kill cells, probably due to a lack of wtp53 [37], but exacerbate the toxicity of Zn^{2+}, indicating death triggered by Zn^{2+} reactivated p53 [27].

3.7. In vivo tumoricidal effect of ZP NPs

To further study the antitumor performance of ZP NPs in vivo, MDA-MB-231 cells were seeded subcutaneously in Balb/c nude mice to establish a xenographic tumor model. Firstly, the distribution of ZP NPs were observed via in vivo fluorescent imaging. After injection of ICG-labeled ZP NPs (NP dose: 6.25 mg/kg), we captured the concentrated ICG signals at time points 12 h to 48 h at the tumor site (Fig. 6A), and the signals were apparently detectable in the ex vivo image of the tumor collected at 48 h post-injection (Fig. 6B). Both results manifested the effective retention of ZP NPs at tumor sites. The photothermal efficacy was then investigated with infrared thermal imaging. The tumor-bearing mice were injected intravenously with saline, PB NPs and ZP NPs (NP dose: 6.25 mg/kg) and the tumor sites were irradiated with an 808 nm laser (1.0 W/cm²). The images and recorded temperature of tumors in PB and ZP groups exhibited an apparently fast elevation than those of the saline group (Fig. 6C and S7), indicating hyperthermia
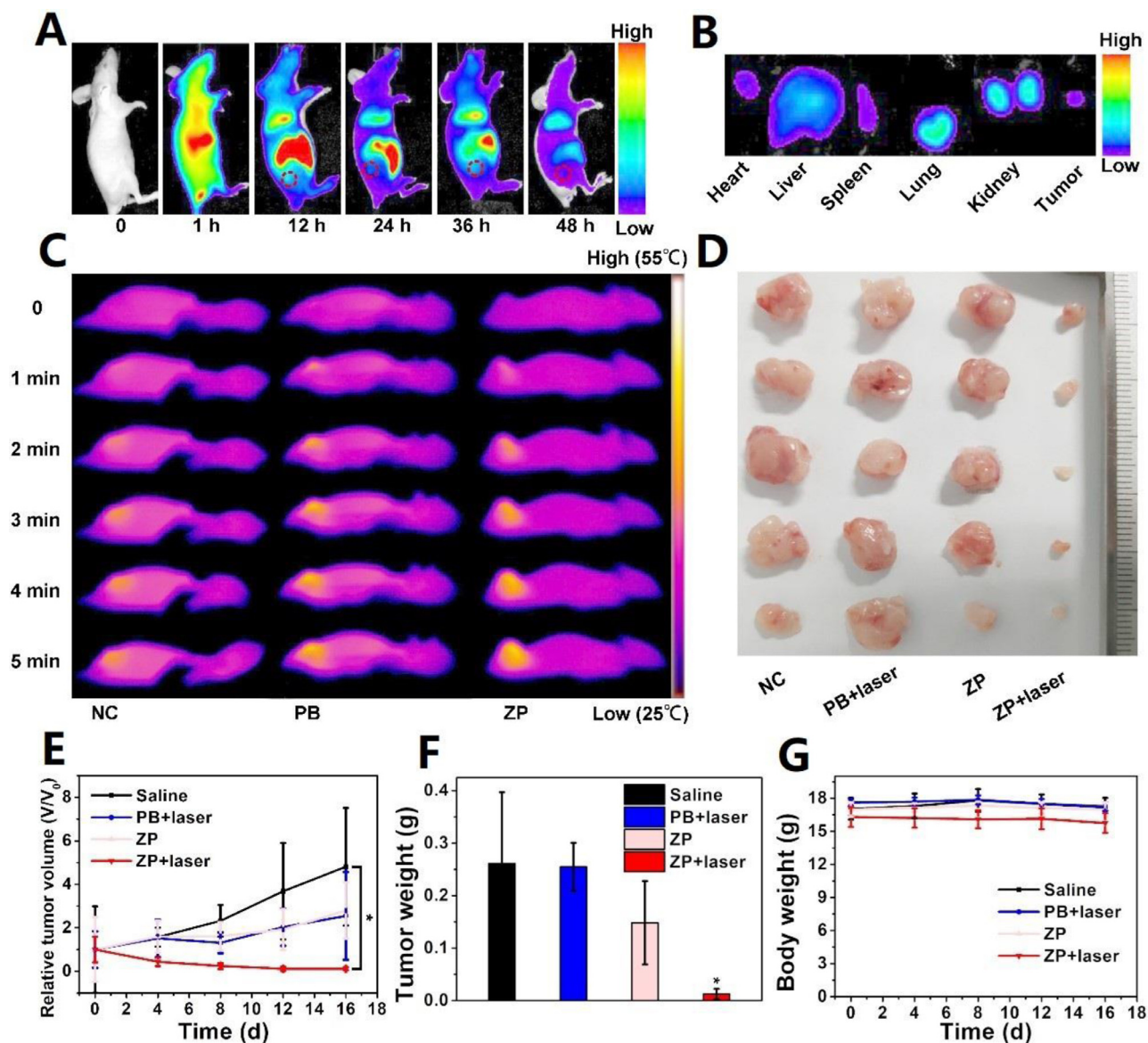
Fig. 6 – *In vivo* ZP treatment on tumor-bearing mice. (A) *In vivo* fluorescent imaging of MDA-MB-231 bearing-mice injected with ICG-labeled ZP NPs. (B) Fluorescent images of major organs collect from a mouse 48 h post-injection of ICG-labeled ZP NPs. (C) IR images taken every minute for tumor-site irradiated mice (100 μg/ml PB or ZP, 24 h). (D) Images of tumors. (E) Changes of relative tumor sizes. $n = 5$. *$P < 0.05$. Student's *t*-test. (F) Tumor weights after treatments. $n = 5$. *$P < 0.05$. Comparing to the saline group, student's *t*-test. (G) Body weight changes. $n = 5$.

created by NPs accumulated at tumor sites under laser treatment.

A 2-week treatment was also performed within 4 randomly divided mice groups: saline, PB + laser, ZP and ZP + laser. The treatment session began at the 7th day after tumor implantation. Agents were delivered every 4 d via intravenous injection to correspondent group of mice (NP dose: 6.25 mg/kg) and laser treatment was performed to PB+laser and ZP+laser groups at 24 h post-injection. The body weights and tumor sizes were measured every 4 d. The mice were sacrificed at the 16th and tumor weights were measured. In relative tumor size data, both PB plus laser treatment group and ZP group displayed slight tumor ablation (Fig. 6D-6F), which seemed less remarkable in tumor weights and pictures probably due a

varied distribution of starting tumor sizes. All three figures, however, consistently demonstrated the best tumoricidal effect of ZP + laser treatment, namely, the combination of zinc delivery and PTT. None of the 4 groups displayed significant body weight fluctuation (Fig. 6G). Little pathological changes were spotted in H&E stained samples from main organs (**Fig. S8**), manifesting relative safety of the treatment.

4. Conclusions

To summarize, with ZP NPs as zinc ion carriers and photothermal agents, we were able to deliver Zn^{2+} with PB and reveal combinational therapeutic effects of Zn^{2+}

and NIR laser triggered hyperthermia in mutp53 containing MDA-MB-231 cells *in vitro* and *in vivo*. Zn^{2+} was doped in PB frameworks via substitution while maintaining the original photothermal ability of PB. ZP NPs collapsed and released Zn^{2+} in a GSH concentration sensitive manner in a neutral environment. Released Zn^{2+}, subsequently, triggered autophagic degradation of mutp53 and apoptotic cell death, and laser treatment accelerated mutp53 abrogation and augmented the cytotoxicity. A decent tumoricidal effect combining Zn^{2+} delivery and PTT was also rendered in the mouse subcutaneous tumor model. ZP NPs were elucidated to be a zinc delivery carrier treating tumors, especially mutp53 carrying tumors, and hence, a promising antitumoral nanomaterial.

Conflicts of interest

The authors declare that they have no known competing financial interests or personal relationships that could have appeared to influence the work reported in this paper.

Acknowledgements

Supplementary materials

Supplementary material associated with this article can be found, in the online version, at doi:10.1016/j.ajps.2022.07.003.

REFERENCES

[1] Vousden KH, Lane DP. p53 in health and disease. Nat Rev Mol Cell Biol 2007;8(4):275–83.
[2] Kruiswijk F, Labuschagne CF, Vousden KH. p53 in survival, death and metabolic health: a lifeguard with a licence to kill. Nat Rev Mol Cell Biol 2015;16(7):393–405.
[3] Joerger AC, Fersht AR. The p53 pathway: origins, inactivation in cancer, and emerging therapeutic approaches. Annu Rev Biochem 2016;85:375–404.
[4] Lane DP. Cancer. p53, guardian of the genome. Nature 1992;358(6381):15–6.
[5] Kandoth C, McLellan MD, Vandin F, Ye K, Niu B, Lu C, et al. Mutational landscape and significance across 12 major cancer types. Nature 2013;502(7471):333–9.
[6] Dolgin E. The most popular genes in the human genome. Nature 2017;551(7681):427–31.
[7] Schulz-Heddergott R, Moll UM. Gain-of-Function (GOF) mutant p53 as actionable therapeutic target. Cancers 2018;10(6).
[8] Zhang C, Liu J, Xu D, Zhang T, Hu W, Feng Z. Gain-of-function mutant p53 in cancer progression and therapy. J Mol Cell Biol 2020;12(9):674–87.
[9] Brosh R, Rotter V. When mutants gain new powers: news from the mutant p53 field. Nat Rev Cancer 2009;9(10):701–13.
[10] Freed-Pastor WA, Prives C. Mutant p53: one name, many proteins. Genes Dev 2012;26(12):1268–86.

[11] Muller PA, Vousden KH. p53 mutations in cancer. Nat Cell Biol 2013;15(1):2–8.
[12] Bossi G, Lapi E, Strano S, Rinaldo C, Blandino G, Sacchi A. Mutant p53 gain of function: reduction of tumor malignancy of human cancer cell lines through abrogation of mutant p53 expression. Oncogene 2006;25(2):304–9.
[13] Vikhanskaya F, Lee MK, Mazzoletti M, Broggini M, Sabapathy K. Cancer-derived p53 mutants suppress p53-target gene expression–potential mechanism for gain of function of mutant p53. Nucleic Acids Res 2007;35(6):2093–104.
[14] Alexandrova EM, Yallowitz AR, Li D, Xu S, Schulz R, Proia DA, et al. Improving survival by exploiting tumour dependence on stabilized mutant p53 for treatment. Nature 2015;523(7560):352–6.
[15] Bykov VJN, Eriksson SE, Bianchi J, Wiman KG. Targeting mutant p53 for efficient cancer therapy. Nat Rev Cancer 2018;18(2):89–102.
[16] Sabapathy K, Lane DP. Therapeutic targeting of p53: all mutants are equal, but some mutants are more equal than others. Nat Rev Clin Oncol 2018;15(1):13–30.
[17] Yan W, Zhang Y, Zhang J, Liu S, Cho SJ, Chen X. Mutant p53 protein is targeted by arsenic for degradation and plays a role in arsenic-mediated growth suppression. J Biol Chem 2011;286(20):17478–86.
[18] Parrales A, Ranjan A, Iyer SV, Padhye S, Weir SJ, Roy A, et al. DNAJA1 controls the fate of misfolded mutant p53 through the mevalonate pathway. Nat Cell Biol 2016;18(11):1233–43.
[19] Zhang S, Zhou L, Hong B, van den Heuvel AP, Prabhu VV, Warfel NA, et al. Small-molecule NSC59984 restores p53 pathway signaling and antitumor effects against colorectal cancer via p73 activation and degradation of mutant p53. Cancer Res 2015;75(18):3842–52.
[20] Li D, Marchenko ND, Schulz R, Fischer V, Velasco-Hernandez T, Talos F, et al. Functional inactivation of endogenous MDM2 and CHIP by HSP90 causes aberrant stabilization of mutant p53 in human cancer cells. Mol Cancer Res 2011;9(5):577–88.
[21] Proia DA, Bates RC. Ganetespib and HSP90: translating preclinical hypotheses into clinical promise. Cancer Res 2014;74(5):1294–300.
[22] Padmanabhan A, Candelaria N, Wong KK, Nikolai BC, Lonard DM, O'Malley BW, et al. USP15-dependent lysosomal pathway controls p53-R175H turnover in ovarian cancer cells. Nat Commun 2018;9(1):1270.
[23] Foggetti G, Ottaggio L, Russo D, Mazzitelli C, Monti P, Degan P, et al. Autophagy induced by SAHA affects mutant P53 degradation and cancer cell survival. Biosci Rep 2019;39(2).
[24] Foggetti G, Ottaggio L, Russo D, Monti P, Degan P, Fronza G, et al. Gambogic acid counteracts mutant p53 stability by inducing autophagy. Biochim Biophys Acta Mol Cell Res 2017;1864(2):382–92.
[25] Garufi A, Pistritto G, Cirone M, D'Orazi G. Reactivation of mutant p53 by capsaicin, the major constituent of peppers. J Exp Clin Cancer Res 2016;35(1):136.
[26] Loh SN. The missing zinc: p53 misfolding and cancer. Metallomics 2010;2(7):442–9.
[27] Meplan C, Richard MJ, Hainaut P. Metalloregulation of the tumor suppressor protein p53: zinc mediates the renaturation of p53 after exposure to metal chelators *in vitro* and in intact cells. Oncogene 2000;19(46):5227–36.
[28] Puca R, Nardinocchi L, Porru M, Simon AJ, Rechavi G, Leonetti C, et al. Restoring p53 active conformation by zinc increases the response of mutant p53 tumor cells to anticancer drugs. Cell Cycle 2011;10(10):1679–89.
[29] Garufi A, Pucci D, D'Orazi V, Cirone M, Bossi G, Avantaggiati ML, et al. Degradation of mutant p53H175

protein by Zn(II) through autophagy. Cell Death Dis 2014;5:e1271.

[30] Liu Y, Wang Y, Song S, Zhang H. Cancer therapeutic strategies based on metal ions. Chem Sci 2021;12(37):12234–47.

[31] Setyawati MI, Tay CY, Leong DT. Effect of zinc oxide nanomaterials-induced oxidative stress on the p53 pathway. Biomaterials 2013;34(38):10133–42.

[32] Garufi A, Trisciuoglio D, Porru M, Leonetti C, Stoppacciaro A, D'Orazi V, et al. A fluorescent curcumin-based Zn(II)-complex reactivates mutant (R175H and R273H) p53 in cancer cells. J Exp Clin Cancer Res 2013;32:72.

[33] Garufi A, Federici G, Gilardini Montani MS, Crispini A, Cirone M, D'Orazi G. Interplay between endoplasmic reticulum (ER) stress and autophagy induces mutant p53H273 degradation. Biomolecules 2020;10(3).

[34] Qian J, Zhang W, Wei P, Yao G, Yi T, Zhang H, et al. Enhancing chemotherapy of p53-mutated cancer through ubiquitination-dependent proteasomal degradation of mutant p53 proteins by engineered ZnFe-4 nanoparticles. Adv Funct Mater 2020;30(40).

[35] Zhang Y, Huang X, Wang L, Cao C, Zhang H, Wei P, et al. Glutathionylation-dependent proteasomal degradation of wide-spectrum mutant p53 proteins by engineered zeolitic imidazolate framework-8. Biomaterials 2021;271: 120720.

[36] Beik J, Abed Z, Ghoreishi FS, Hosseini-Nami S, Mehrzadi S, Shakeri-Zadeh A, et al. Nanotechnology in hyperthermia cancer therapy: from fundamental principles to advanced applications. J Control Release 2016;235:205–21.

[37] Ohnishi K, Ohnishi T. Heat-induced p53-dependent signal transduction and its role in hyperthermic cancer therapy. Int J Hyperthermia 2001;17(5):415–27.

[38] Wang L, Lin X, Wang J, Hu Z, Ji Y, Hou S, et al. Novel insights into combating cancer chemotherapy resistance using a plasmonic nanocarrier: enhancing drug sensitiveness and accumulation simultaneously with localized mild photothermal stimulus of femtosecond pulsed laser. Adv Funct Mater 2014;24(27):4229–39.

[39] Shokouhimehr M, Soehnlen ES, Hao J, Griswold M, Flask C, Fan X, et al. Dual purpose Prussian blue nanoparticles for cellular imaging and drug delivery: a new generation of T1-weighted MRI contrast and small molecule delivery agents. J Mater Chem 2010;20(25).

[40] Aaseth J, Nurchi VM, Andersen O. Medical therapy of patients contaminated with radioactive cesium or iodine. Biomolecules 2019;9(12).

[41] Wang X, Cheng L. Multifunctional Prussian blue-based nanomaterials: preparation, modification, and theranostic applications. Coord Chem Rev 2020:419.

[42] Fu G, Liu W, Feng S, Yue X. Prussian blue nanoparticles operate as a new generation of photothermal ablation agents for cancer therapy. Chem Commun 2012;48(94):11567–9.

[43] Wu W, Yu L, Pu Y, Yao H, Chen Y, Shi J. Copper-enriched prussian blue nanomedicine for in situ disulfiram toxification and photothermal antitumor amplification. Adv Mater 2020;32(17):e2000542.

[44] Zuo W, Fan Z, Chen L, Liu J, Wan Z, Xiao Z, et al. Copper-based theranostic nanocatalysts for synergetic photothermal-chemodynamic therapy. Acta Biomater 2022.

[45] Chen Y, Li ZH, Pan P, Hu JJ, Cheng SX, Zhang XZ. Tumor-microenvironment-triggered ion exchange of a metal-organic framework hybrid for multimodal imaging and synergistic therapy of tumors. Adv Mater 2020;32(24):e2001452.

[46] Buser HJ, Schwarzenbach D, Petter W, Ludi A. The crystal structure of Prussian Blue: Fe4[Fe(CN)6]3.xH2O. Inorg Chem 1977;16(11):2704–10.

[47] Li J, Liu X, Tan L, Cui Z, Yang X, Liang Y, et al. Zinc-doped Prussian blue enhances photothermal clearance of Staphylococcus aureus and promotes tissue repair in infected wounds. Nat Commun 2019;10(1):4490.

[48] Schafer FQ, Buettner GR. Redox environment of the cell as viewed through the redox state of the glutathione disulfide/glutathione couple. Free Radic Biol Med 2001;30(11):1191–212.

[49] Fuhr BJ, Rabenstein DL. Nuclear magnetic resonance studies of the solution chemistry of metal complexes. IX. The binding of cadmium, zinc, lead, and mercury by glutathione. J Am Chem Soc 1973;95(21):6944–50.

[50] Choudhury S, Kolukula VK, Preet A, Albanese C, Avantaggiati ML. Dissecting the pathways that destabilize mutant p53: the proteasome or autophagy? Cell Cycle 2013;12(7):1022–9.

[51] He H, Liu L, Zhang S, Zheng M, Ma A, Chen Z, et al. Smart gold nanocages for mild heat-triggered drug release and breaking chemoresistance. J Control Release 2020;323:387–97.